Appendix B. Supplementary sections and data

B1. Outline of Appendix B

Appendix B contains three Sections (B2, B3, and B4) that supplement the results outlined in the main text. Tables B1 and B4 also provide the input parameters used in the modelling during this study, with Fig. B1 showing peridotite solidi as a function of pressure and water abundance. The distribution of different Grüneisen parameters in the mantle is shown in Fig. B2, and the results described in the main text are supplemented by Figs B3 through B11 and Tables B2 and B3.

B2. Total temperature drop and continental crustal growth

The evolution of T_{mean} for the 11 realistic runs is shown in Fig. B10, with Table B3 providing mean mantle temperatures $T_{mean,beg}$ at $\tau = 4490$ Ma, $T_{mean,end}$ at the present day, and the temperature drop, ΔT_{mean} for the runs shown in Figs 1–3 and B10. The average theoretical temperature drop is 210 K. van Hunen et al. (2008) suggested a decrease of 100–300 K in mantle potential temperature since the Archean. Many other authors have arrived at similar conclusions although the mechanisms invoked differ. Davies (2006, 2007) suggested early depletion of the upper mantle and Archean oceanic crust thicknesses that were similar to those of the present day but with a reduced thermal boundary layer thickness, meaning less subduction took place. In contrast, van Hunen and van den Berg (2008) proposed that the higher mantle temperatures in the Archean caused a lowering of viscosity and an increase in the degree of partial melting of the mantle, yielding thicker harzburgitic layers within the lower part of the oceanic lithosphere, a feature that again impeded the initiation of subduction. The lower viscosity of the mantle during the Archean also increased the frequency of slab breakoff events. Both of these subduction mechanisms would have caused mantle cooling to temperatures lower than those suggested by simpler models. van Hunen et al. (2008) concluded that the efficiency of plate tectonics was significantly reduced with a mantle that had a 200 K higher ambient mantle temperature than is the case for the present day. The model of Labrosse and Jaupart (2007) shows a modest mantle temperature decline of 150 K over the past 3000 Ma, with a simplistic and linear extrapolation over the past 4490 Ma yielding a temperature decrease of 225 K. This is close to the 210 K obtained in our modelling although the structure of the two models

is very different. Stacey and Davis (2009) suggested that the decrease in temperature at the core–mantle boundary (T_c) was smaller than or equal to 200 K, and Nakagawa and Tackley (2012) suggested a mantle cooling rate of 70 K/Ga. A straightforward linear extrapolation over 4490 Ma yields a 314 K temperature decrease. Overall, recent modelling suggests that T_{mean} decreases were lower than those suggested by earlier parameterized thermal evolution models, with the more recent predictions of ΔT_{mean} values roughly agreeing with the ΔT_{mean}=210 K value obtained in the present study.

We have already emphasised that the E_{kin}, *qob* and magmatic activity curves are not *strictly* periodically distributed. The evolution of the system caused by radioactive decay and other irreversible processes does lead to a decrease in the volumetrically averaged mantle temperature (Fig. B10) and the associated peaks of juvenile magmatic activity from 2000 Ma onwards (Fig. 3).

Taylor and McLennan (2009) concluded that 50%–70% of the continental crust had formed by the end of the late Archean, similar to the results of the present modelling (Fig. 3), which shows that, on average, 66.77% of the present continental mass existed at τ = 2.5 Ga (cf. Table B2, 8th column). Dhuime et al. (2012) reached a similar conclusion whereby 65% of the present continental mass was present at τ = 2.5 Ga. The quantity p_{t25} denotes the percentage of continental mass that was developed by τ=2500 Ma. In contrast to the thermal and creep-mechanical based predictions, chemical differentiation models yield a greater stochastic contribution (Walzer et al., 2009).

Our trendline of integrated continental volumes (Fig. B11) compares well with observation-based studies (e.g., GLAM, Begg et al., 2009; Belousova et al., 2010; Dhuime et al., 2012). However, our data also provide a different view of the episodicity of continental growth (cf. Fig. 3), primarily as none of our results showed the continuous or near-continuous generation of continental crustal material. The underlying reason for this episodicity is complex. One important control is the reduction of volatile abundances in partly melted material by differentiation, where continuing differentiation can lead to a sudden increase in volcanism. The escape of a huge amount of water from a source region leads to a rapid increase in the solidus temperature in the source region, thereby initiating a post-paroxysmal time of regional quiescence. The initiation of modern-type oceanic lithospheric subduction at τ=3.0 Ga would have generated more or less steady oceanic plate motions. Nevertheless, secondary accretion-related oscillations of continental

growth are present as a result of the occasional accretion of oceanic plateaus (Martin et al., 2014) or arcs (Davidson and Arculus, 2006) to continents.

Figures 3 and B11, and Table B2 (8th column) indicate that between 60.4% and 75.7% of present-day continental mass was in place at τ=2500 Ma. Griffin et al. (2010) suggested that the compositions of xenoliths from the subcontinental lithospheric mantle (SCLM) broadly correlate with the tectonothermal age of the overlaying continent. Modelling zircon Hf isotope data of the database GEOROC (Geochemistry of Rocks of the Oceans and Continents) suggests that about 70% of continental mass was generated by τ=2500 Ma (Belousova et al., 2009), which is consistent with our modelling results.

B3. Heat flow at the core–mantle boundary

The flux of heat flow at the core–mantle boundary (CMB) remains controversial, with Monnereau and Yuen (2010) deriving a present-day total CMB heat flow ($q_{c,t0}$ in our notation) of 5 TW assuming a thermal mantle conductivity of k = 5 W/(m·K). In comparison, Davies (1988) and Sleep (1990) derived a value of $q_{c,t0}$ = 3.5 TW from swell topography. Our research yields $q_{c,t9}$ values between 2.651 and 3.617 TW, where $q_{c,t9}$ is the total CMB heat flow averaged over the last 900 Ma (cf. Table B2, 7th column). This corresponds to CMB heat flows (q_{c9}) of between 17.42 and 23.77 mW/m^2 (cf. Table B2, third column). Nakagawa and Tackley (2015) obtained a final total CMB heat flow ($q_{c,t0}$) of 5 TW for mobile-lid and stagnant-lid cases, with the former being similar to the present-day Earth assuming a reference density structure of the core similar to the preliminary reference Earth model PREM (Dziewonski and Anderson, 1981). Calculated present-day $q_{c,t0}$ values are higher (between 5 and 14 TW) as a result of allocating significant proportions of U, Th, and K into the core in order to circumvent the cumbersome ^{40}Ar problem. However, iron meteorites do not contain appreciable amounts of U, Th, or K, meaning that we should not exclude the possibility that the present-day core is nearly radionuclide-free. However, if $q_{c,t0} < 2$ TW, the net entropy contribution (Nimmo, 2007) would become negative, making any dynamo impossible. This means that $q_{c,t0}$ must range between 2 and 14 TW. Nevertheless, plumes would be possible even if $q_{c,t0} = 2$ TW if there was a heat producing element-rich layer just above the CMB. The requirements to power the dynamo are low, with Christensen and Tilgner (2004) suggesting values between 0.2 and 0.5 TW. In addition, attempting to resolve this prob-

lem by increasing the primordial heat in the core leads to other difficulties (see Appendix C).

B4. Future research

This section focuses on the shortcomings and simplifications involved in our modelling, in order to propose future improvements to this approach. We believe that the essential features of our viscosity function η_4 (cf. Fig. B8) are realistic. In particular, the assumed high-viscosity transition layer is expected to be strengthened by plate-tectonic-driven convection as cold slabs stagnate in the transition layer, leaving behind garnet-rich material. However, the assumed general level of viscosity is somewhat too high; this assumption is necessary for numerical reasons because Rayleigh number values decrease as a function of time as a result of diminishing radiogenic heat production and cooling of the mantle. The somewhat too low rms surface velocity is immediately connected to this shortcoming and can be surmounted only by an essential numerical improvement of the Terra code. However, despite this imperfection our model significantly improves on both parameterised Earth evolution and conceptual models in that it has a physical basis and can quantitatively explain a number of features of the chemical and thermal evolution of the Earth.

Our model also demonstrates that periods of quiescence between peaks in magmatic activity are essentially caused by the dependence of the peridotite solidus on water abundance. However, our model does not include the full mantle deep-water cycle, making this one of the most important tasks to be undertaken in future research.

We modelled the accretion of continental material to the continents but did not make any assumptions regarding the number, size, form, and distribution of the computed continents. Some previous modelling aimed to reproduce the observed total topography of the Earth in terms of spherical harmonics (Walzer and Hendel, 2008). In addition, our modelling included oceanic but not continental rifting; consequently, the inclusion of both processes is a future task for research related to this approach.

We also considered thermal conductivity k to be constant but varied the constant from case to case. A value of k = 5 W/(m·K) worked best with our models, although one way of improving this would be to introduce a depth-dependent k; however, this would be only a minor improvement in

comparison with any possible improvements in the viscosity function used in our model.

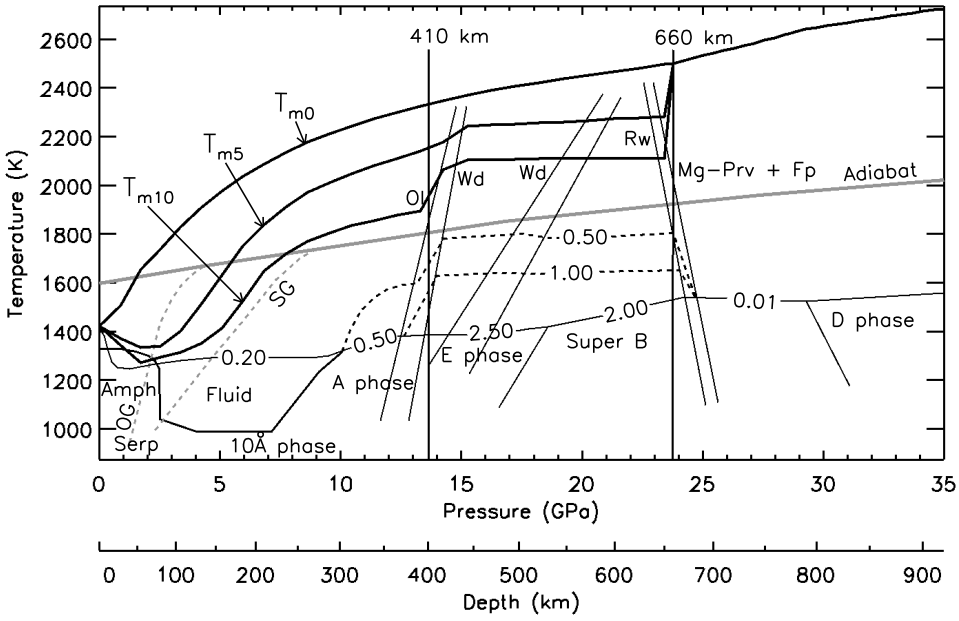

Fig. B1. Variations in peridotite solidi (T_{sol}) as a function of pressure (P) and water abundance; modified from Litasov (2011). The curve for 0 ppm H_2O is denoted by T_{m0}, for 500 ppm H_2O by T_{m5}, and for 1000 ppm H_2O by T_{m10}. Ol = olivine, Wd = wadsleyite, Rw = ringwoodite, Mg-Prv = magnesium perovskite, Fp = ferropericlase. The MORB adiabat at a potential temperature of 1588 K is labelled "Adiabat".

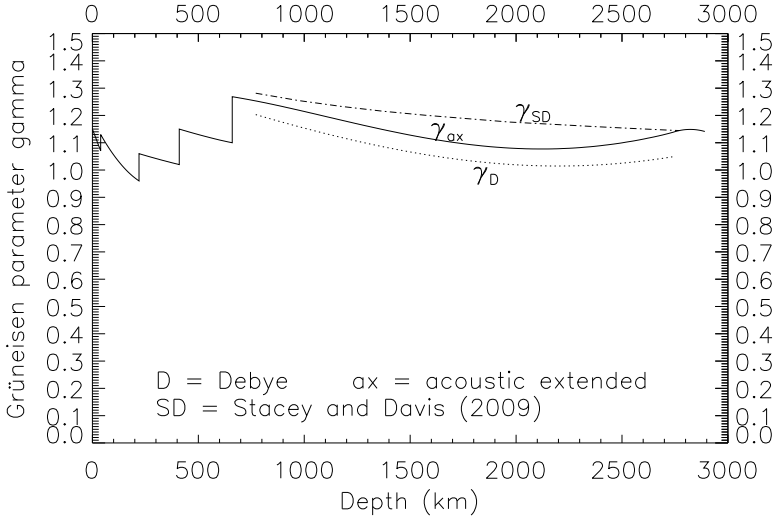

Fig. B2. Comparison of different Grüneisen parameters (γ) as a function of depth (h). The γ values according to Stacey and Davis (2009) are denoted by γ_{SD}, with our newly extended acoustic gamma values denoted by γ_{ax}, and Debye gamma values denoted by γ_D.

Table B1.

Physical properties of the mantle as a function of depth (h). The extended acoustic Grüneisen parameter (γ_{ax}) and Debye gamma (γ_D) values were determined using PREM observational values. The Grüneisen parameter of Stacey and Davis (2009) is indicated by γ_{SD}. The quantity T_{m0} denotes the dry peridotite solidus with T_{m5} and T_{m10} indicating the solidus of peridotite containing 500 ppm H_2O and 1000 ppm H_2O, respectively (Litasov, 2011). The viscosity profile factor of Eq.(5) is indicated by η_4, with T_{ad} indicating the adiabatic temperature of the mantle, α representing thermal expansivity, and c_p indicating specific heat values at a constant pressure. NaN means "Not a Number" as is customary in information technology.

h(km)	γ_{ax}	γ_{D}	γ_{SD}	T_{m0}(K)	T_{m5}(K)	T_{m10}(K)	log(η_4) (Pa•s)	T_{ad}(K)	α ($10^{-6}K^{-1}$)	cp (J/(kg•K))
0	1.1500	2.8689	-0.6467	1422.8	1422.8	1422.8	24.000	1601.2	40.000	695.2
10	1.1295	2.8701	-0.6485	1452.6	1404.7	1395.1	24.000	1605.2	43.333	766.8
20	1.1090	2.8714	-0.6496	1482.4	1386.6	1367.4	24.000	1609.2	46.667	1092.4
30	1.0885	2.8727	-0.9995	1516.2	1369.1	1339.7	24.000	1615.3	50.000	1785.0
39	1.0700	2.8738	-1.0013	1567.2	1356.1	1314.8	23.782	1624.6	53.000	1922.3
39	1.1300	2.8738	-1.0013	1567.2	1356.1	1314.8	23.782	1624.6	33.500	1150.5
40	1.1286	2.8739	-1.0015	1572.9	1354.7	1312.0	23.758	1625.1	33.477	1150.9
50	1.1153	2.8752	-1.0034	1629.5	1340.3	1284.3	23.516	1630.4	33.249	1155.1
60	1.1024	2.8765	-1.0052	1673.0	1334.9	1276.7	23.274	1637.4	33.027	1159.1
70	1.0900	2.8777	-1.0071	1705.8	1336.9	1285.1	23.032	1643.5	32.810	1162.9
80	1.0781	2.8790	-1.0089	1738.6	1338.9	1293.6	22.789	1648.2	32.598	1166.5
80	1.0781	2.8790	-1.0266	1738.6	1338.9	1293.6	22.789	1648.2	32.598	1166.5
90	1.0666	2.8803	-1.0265	1772.8	1361.9	1302.0	22.547	1653.0	32.392	1169.9
100	1.0556	2.8815	-1.0264	1807.1	1385.8	1310.5	22.305	1657.7	32.191	1173.0
110	1.0451	2.8828	-1.0264	1840.0	1416.6	1320.7	22.063	1662.4	31.996	1176.0
120	1.0350	2.8841	-1.0264	1870.3	1459.4	1334.2	21.821	1667.0	31.806	1178.6
130	1.0254	2.8854	-1.0264	1900.6	1502.1	1347.6	21.579	1671.9	31.621	1181.0
140	1.0163	2.8866	-1.0265	1928.2	1547.2	1369.1	21.337	1676.3	31.441	1183.2
150	1.0076	2.8879	-1.0266	1955.1	1592.9	1392.9	21.095	1680.2	31.267	1185.0
160	0.9994	2.8892	-1.0267	1981.1	1638.7	1420.3	20.853	1684.3	31.099	1186.6
170	0.9917	2.8905	-1.0269	2003.5	1684.9	1463.0	20.611	1688.6	30.936	1187.8
180	0.9844	2.8918	-1.0271	2025.8	1731.2	1505.7	20.368	1692.9	30.778	1188.7
190	0.9776	2.8931	-1.0274	2047.0	1770.4	1551.7	20.126	1697.4	30.625	1189.3
200	0.9713	2.8944	-1.0277	2067.4	1804.7	1599.9	19.884	1701.6	30.478	1189.6
210	0.9654	2.8957	-1.0280	2087.8	1839.0	1648.2	19.642	1705.4	30.336	1189.5
220	0.9600	2.8970	-1.0284	2106.2	1867.3	1676.1	19.400	1708.8	30.200	1189.1
220	1.0600	1.2321	1.0323	2106.2	1867.3	1676.1	19.400	1708.8	28.800	1209.1
230	1.0577	1.2322	1.0346	2124.6	1895.7	1703.9	19.432	1712.7	28.584	1209.2
240	1.0554	1.2322	1.0368	2142.0	1921.6	1728.3	19.463	1717.1	28.370	1209.3
250	1.0531	1.2323	1.0391	2157.9	1944.0	1747.7	19.495	1721.1	28.156	1209.3
260	1.0509	1.2324	1.0413	2173.8	1966.3	1767.1	19.526	1724.8	27.944	1209.3
270	1.0487	1.2325	1.0436	2188.1	1983.1	1781.3	19.558	1729.5	27.733	1209.2
280	1.0465	1.2325	1.0459	2202.0	1998.5	1794.2	19.589	1734.1	27.523	1209.0
290	1.0443	1.2326	1.0482	2215.5	2013.5	1806.8	19.621	1738.6	27.314	1208.8
300	1.0421	1.2327	1.0504	2227.4	2027.5	1818.2	19.653	1742.8	27.106	1208.5
310	1.0400	1.2328	1.0527	2239.3	2041.4	1829.6	19.684	1746.4	26.900	1208.2
320	1.0379	1.2328	1.0550	2251.0	2054.7	1838.9	19.716	1750.3	26.695	1207.8
330	1.0358	1.2329	1.0573	2262.4	2067.6	1846.9	19.747	1754.4	26.491	1207.3
340	1.0338	1.2330	1.0596	2273.8	2080.5	1854.8	19.779	1758.1	26.288	1206.8
350	1.0317	1.2331	1.0618	2284.2	2092.4	1863.3	19.811	1762.0	26.086	1206.2
360	1.0297	1.2331	1.0641	2294.7	2104.4	1871.7	19.842	1766.1	25.885	1205.6
370	1.0277	1.2332	1.0664	2304.5	2115.8	1879.3	19.874	1770.0	25.686	1204.9
380	1.0258	1.2333	1.0687	2313.4	2126.8	1885.8	19.905	1773.7	25.488	1204.2
390	1.0238	1.2334	1.0710	2322.3	2137.7	1892.2	19.937	1777.5	25.291	1203.4
400	1.0219	1.2334	1.0733	2331.3	2151.6	1949.1	19.968	1781.3	25.095	1202.5
410	1.0200	1.2335	1.0756	2340.2	2166.0	2015.2	20.000	1798.1	24.900	1201.6
410	1.1500	2.0697	3.2953	2340.2	2166.0	2015.2	20.000	1798.1	27.400	1228.0
420	1.1477	2.0654	3.3185	2349.1	2183.2	2068.4	20.684	1821.0	26.997	1225.5
430	1.1454	2.0612	3.3416	2357.5	2208.5	2083.3	21.368	1830.1	26.603	1223.0
440	1.1431	2.0570	3.3647	2366.0	2233.9	2098.2	22.052	1833.8	26.218	1220.6
450	1.1409	2.0528	3.3877	2374.1	2243.8	2103.7	22.736	1837.4	25.842	1218.3
460	1.1387	2.0487	3.4107	2382.0	2245.8	2104.2	22.736	1840.6	25.475	1216.0
470	1.1365	2.0447	3.4336	2389.9	2247.8	2104.7	22.736	1843.7	25.118	1213.9
480	1.1343	2.0406	3.4565	2396.4	2249.3	2105.2	22.736	1846.6	24.770	1211.9
490	1.1321	2.0367	3.4793	2402.8	2250.8	2105.6	22.736	1850.0	24.430	1210.0
500	1.1300	2.0328	3.5021	2409.0	2252.3	2106.4	22.736	1854.2	24.100	1208.3
510	1.1279	2.0289	3.5248	2415.0	2253.8	2107.4	22.736	1858.1	23.779	1206.7
520	1.1258	2.0250	3.5474	2421.0	2255.2	2108.4	22.736	1862.4	23.467	1205.3
520	1.1258	2.0250	3.5474	2421.0	2255.2	2108.4	22.736	1862.4	23.467	1205.3
530	1.1238	2.0213	3.5700	2426.9	2257.2	2108.9	22.736	1871.3	23.164	1204.0
540	1.1217	2.0175	3.5926	2432.9	2259.2	2109.4	22.736	1881.1	22.871	1203.0
550	1.1197	2.0138	3.6151	2438.9	2261.1	2109.8	22.736	1892.0	22.586	1202.1
560	1.1177	2.0101	3.6376	2444.8	2263.1	2109.8	22.736	1903.1	22.310	1201.5
570	1.1158	2.0065	3.6600	2450.8	2265.1	2109.8	22.736	1905.2	22.044	1201.1

h(km)	γ_{ax}	γ_{D}	γ_{SD}	T_{m0}(K)	T_{m5}(K)	T_{m10}(K)	log(η_4) (Pa•s)	T_{ad}(K)	α ($10^{-6}K^{-1}$)	cp (J/(kg•K))
580	1.1138	2.0029	3.6824	2456.5	2267.8	2109.8	22.736	1906.8	21.787	1201.0
590	1.1119	1.9994	3.7047	2462.1	2270.8	2109.8	22.736	1907.6	21.539	1201.1
600	1.1100	1.9958	3.7270	2467.6	2273.6	2109.8	22.736	1909.3	21.300	1201.5
600	1.1100	2.7450	0.6063	2467.6	2273.6	2109.8	22.736	1909.3	21.300	1201.5
610	1.1082	2.7430	0.6054	2473.2	2275.1	2109.8	22.280	1911.5	21.132	1197.7
620	1.1065	2.7410	0.6044	2478.8	2276.6	2109.8	21.824	1914.1	20.985	1195.1
630	1.1048	2.7390	0.6035	2484.4	2278.1	2109.8	21.368	1916.3	20.858	1193.5
640	1.1032	2.7370	0.6025	2489.9	2279.6	2109.8	20.912	1918.0	20.752	1192.9
650	1.1016	2.7350	0.6016	2495.5	2281.1	2109.8	20.456	1920.8	20.666	1193.5
660	1.1000	2.7331	0.6007	2501.1	2501.1	2501.1	20.000	1918.7	20.600	1195.2
660	1.2686	3.6735	0.9591	2501.1	NaN	NaN	20.000	1918.7	23.007	1237.9
670	1.2673	3.6691	0.9574	2510.6	NaN	NaN	20.000	1884.9	22.894	1236.8
680	1.2660	3.6646	0.9557	2522.7	NaN	NaN	20.000	1888.5	22.782	1235.7
690	1.2647	3.6602	0.9541	2533.8	NaN	NaN	20.000	1897.9	22.671	1234.7
700	1.2633	3.6558	0.9524	2543.5	NaN	NaN	20.000	1906.6	22.562	1233.7
710	1.2620	3.6515	0.9508	2553.0	NaN	NaN	20.000	1914.3	22.452	1232.7
720	1.2606	3.6472	0.9491	2563.2	NaN	NaN	20.000	1922.1	22.344	1231.7
730	1.2592	3.6430	0.9473	2572.5	NaN	NaN	20.000	1927.5	22.237	1230.8
740	1.2577	3.6388	0.9456	2583.4	NaN	NaN	20.000	1930.4	22.130	1229.8
750	1.2563	3.6346	0.9438	2595.6	NaN	NaN	20.000	1933.7	22.024	1228.9
760	1.2548	3.6305	0.9420	2605.7	NaN	NaN	20.019	1937.5	21.920	1228.1
770	1.2533	3.6264	0.9402	2618.8	NaN	NaN	20.091	1941.3	21.816	1227.2
771	1.2531	3.6260	0.9400	2620.0	NaN	NaN	20.099	1941.7	21.805	1227.1
771	1.2531	1.2031	1.4099	2620.0	NaN	NaN	20.099	1941.7	21.805	1227.1
780	1.2518	1.2010	1.4072	2628.9	NaN	NaN	20.162	1945.4	21.712	1227.7
790	1.2503	1.1988	1.4043	2641.0	NaN	NaN	20.232	1948.4	21.610	1228.4
800	1.2487	1.1965	1.4014	2647.8	NaN	NaN	20.300	1950.5	21.509	1229.0
810	1.2471	1.1943	1.3984	2654.6	NaN	NaN	20.367	1953.9	21.408	1229.7
820	1.2455	1.1921	1.3954	2661.3	NaN	NaN	20.432	1957.3	21.308	1230.4
830	1.2439	1.1898	1.3924	2668.1	NaN	NaN	20.496	1960.7	21.209	1231.0
840	1.2423	1.1876	1.3893	2674.8	NaN	NaN	20.559	1964.0	21.111	1231.7
850	1.2406	1.1854	1.3862	2681.4	NaN	NaN	20.621	1967.4	21.014	1232.4
860	1.2390	1.1832	1.3832	2688.1	NaN	NaN	20.681	1970.7	20.917	1233.1
870	1.2373	1.1810	1.3801	2694.8	NaN	NaN	20.740	1974.1	20.821	1233.8
871	1.2371	1.1808	1.3798	2695.4	NaN	NaN	20.746	1974.4	20.812	1233.9
880	1.2356	1.1789	1.3770	2701.4	NaN	NaN	20.798	1977.4	20.726	1234.5
890	1.2339	1.1767	1.3738	2708.0	NaN	NaN	20.855	1980.7	20.632	1235.2
900	1.2322	1.1745	1.3707	2714.6	NaN	NaN	20.910	1984.0	20.539	1235.9
910	1.2304	1.1724	1.3676	2721.1	NaN	NaN	20.964	1987.3	20.446	1236.7
920	1.2287	1.1703	1.3644	2727.6	NaN	NaN	21.018	1990.5	20.354	1237.4
930	1.2270	1.1681	1.3613	2734.1	NaN	NaN	21.070	1993.8	20.263	1238.1
940	1.2252	1.1660	1.3581	2740.6	NaN	NaN	21.121	1997.1	20.173	1238.8
950	1.2235	1.1639	1.3550	2747.1	NaN	NaN	21.171	2000.3	20.084	1239.5
960	1.2217	1.1618	1.3518	2753.5	NaN	NaN	21.219	2003.5	19.995	1240.3
970	1.2199	1.1597	1.3487	2760.0	NaN	NaN	21.267	2006.7	19.907	1241.0
971	1.2197	1.1595	1.3483	2760.6	NaN	NaN	21.272	2007.1	19.898	1241.1
980	1.2181	1.1576	1.3455	2766.4	NaN	NaN	21.314	2009.9	19.819	1241.7
990	1.2163	1.1556	1.3423	2772.8	NaN	NaN	21.360	2013.1	19.733	1242.5
1000	1.2146	1.1535	1.3391	2779.1	NaN	NaN	21.405	2016.3	19.647	1243.2
1010	1.2127	1.1515	1.3360	2785.4	NaN	NaN	21.449	2019.5	19.562	1243.9
1020	1.2109	1.1494	1.3328	2791.8	NaN	NaN	21.492	2022.6	19.478	1244.7
1030	1.2091	1.1474	1.3296	2798.1	NaN	NaN	21.534	2025.8	19.394	1245.4
1040	1.2073	1.1454	1.3265	2804.3	NaN	NaN	21.575	2028.9	19.311	1246.2
1050	1.2055	1.1434	1.3233	2810.6	NaN	NaN	21.615	2032.0	19.229	1246.9
1060	1.2037	1.1414	1.3201	2816.8	NaN	NaN	21.654	2035.2	19.148	1247.7
1070	1.2019	1.1394	1.3170	2823.0	NaN	NaN	21.693	2038.2	19.067	1248.5
1071	1.2017	1.1392	1.3167	2823.7	NaN	NaN	21.697	2038.6	19.059	1248.5
1080	1.2000	1.1374	1.3138	2829.2	NaN	NaN	21.730	2041.3	18.987	1249.2
1090	1.1982	1.1355	1.3107	2835.4	NaN	NaN	21.767	2044.4	18.908	1250.0
1100	1.1964	1.1335	1.3076	2841.6	NaN	NaN	21.803	2047.5	18.829	1250.8
1110	1.1945	1.1316	1.3044	2847.7	NaN	NaN	21.839	2050.6	18.751	1251.5
1120	1.1927	1.1297	1.3013	2853.8	NaN	NaN	21.873	2053.6	18.674	1252.3
1130	1.1909	1.1278	1.2982	2859.9	NaN	NaN	21.907	2056.7	18.597	1253.1
1140	1.1891	1.1259	1.2951	2866.0	NaN	NaN	21.940	2059.7	18.521	1253.8

h(km)	γ_{ax}	γ_{D}	γ_{SD}	T_{m0}(K)	T_{m5}(K)	T_{m10}(K)	log(η_4) (Pa•s)	T_{ad}(K)	α ($10^{-6}K^{-1}$)	cp (J/(kg•K))
1150	1.1873	1.1240	1.2920	2872.0	NaN	NaN	21.972	2062.7	18.446	1254.6
1160	1.1854	1.1221	1.2890	2878.0	NaN	NaN	22.003	2065.7	18.371	1255.3
1170	1.1836	1.1202	1.2859	2884.1	NaN	NaN	22.034	2068.7	18.297	1256.1
1171	1.1834	1.1200	1.2856	2884.6	NaN	NaN	22.037	2069.0	18.290	1256.2
1180	1.1818	1.1184	1.2829	2890.0	NaN	NaN	22.064	2071.7	18.224	1256.9
1190	1.1800	1.1165	1.2798	2896.0	NaN	NaN	22.093	2074.7	18.151	1257.6
1200	1.1782	1.1147	1.2768	2902.0	NaN	NaN	22.122	2077.7	18.079	1258.4
1210	1.1764	1.1129	1.2738	2907.9	NaN	NaN	22.150	2080.6	18.008	1259.2
1220	1.1746	1.1111	1.2708	2913.8	NaN	NaN	22.178	2083.6	17.937	1259.9
1230	1.1728	1.1093	1.2679	2919.7	NaN	NaN	22.205	2086.5	17.867	1260.7
1240	1.1710	1.1075	1.2649	2925.6	NaN	NaN	22.231	2089.5	17.798	1261.5
1250	1.1692	1.1058	1.2620	2931.4	NaN	NaN	22.256	2092.4	17.729	1262.3
1260	1.1675	1.1040	1.2591	2937.3	NaN	NaN	22.281	2095.3	17.661	1263.0
1270	1.1657	1.1023	1.2562	2943.1	NaN	NaN	22.306	2098.2	17.593	1263.8
1271	1.1655	1.1021	1.2559	2943.7	NaN	NaN	22.308	2098.5	17.586	1263.9
1280	1.1639	1.1005	1.2533	2948.9	NaN	NaN	22.330	2101.1	17.526	1264.6
1290	1.1622	1.0988	1.2504	2954.7	NaN	NaN	22.353	2104.0	17.459	1265.3
1300	1.1604	1.0971	1.2476	2960.5	NaN	NaN	22.376	2106.9	17.394	1266.1
1310	1.1587	1.0955	1.2448	2966.2	NaN	NaN	22.398	2109.8	17.328	1266.9
1320	1.1570	1.0938	1.2420	2971.9	NaN	NaN	22.420	2112.6	17.264	1267.6
1330	1.1553	1.0921	1.2392	2977.7	NaN	NaN	22.441	2115.5	17.200	1268.4
1340	1.1536	1.0905	1.2365	2983.4	NaN	NaN	22.462	2118.3	17.136	1269.1
1350	1.1519	1.0889	1.2338	2989.0	NaN	NaN	22.482	2121.1	17.073	1269.9
1360	1.1502	1.0872	1.2311	2994.7	NaN	NaN	22.502	2124.0	17.011	1270.6
1370	1.1485	1.0856	1.2284	3000.4	NaN	NaN	22.521	2126.8	16.949	1271.4
1371	1.1483	1.0855	1.2282	3000.9	NaN	NaN	22.523	2127.1	16.943	1271.5
1380	1.1468	1.0841	1.2258	3006.0	NaN	NaN	22.540	2129.6	16.888	1272.1
1390	1.1452	1.0825	1.2232	3011.6	NaN	NaN	22.558	2132.4	16.827	1272.8
1400	1.1436	1.0809	1.2206	3017.2	NaN	NaN	22.576	2135.2	16.767	1273.6
1410	1.1419	1.0794	1.2181	3022.8	NaN	NaN	22.593	2138.0	16.707	1274.3
1420	1.1403	1.0779	1.2156	3028.3	NaN	NaN	22.610	2140.8	16.648	1275.0
1430	1.1387	1.0764	1.2131	3033.9	NaN	NaN	22.627	2143.5	16.589	1275.7
1440	1.1371	1.0749	1.2106	3039.4	NaN	NaN	22.643	2146.3	16.531	1276.5
1450	1.1355	1.0734	1.2082	3044.9	NaN	NaN	22.659	2149.1	16.474	1277.2
1460	1.1340	1.0719	1.2058	3050.4	NaN	NaN	22.674	2151.8	16.417	1277.9
1470	1.1324	1.0705	1.2034	3055.9	NaN	NaN	22.690	2154.5	16.360	1278.6
1471	1.1323	1.0703	1.2032	3056.5	NaN	NaN	22.691	2154.8	16.355	1278.6
1480	1.1309	1.0690	1.2011	3061.4	NaN	NaN	22.704	2157.3	16.304	1279.3
1490	1.1294	1.0676	1.1988	3066.8	NaN	NaN	22.718	2160.0	16.249	1279.9
1500	1.1279	1.0662	1.1965	3072.3	NaN	NaN	22.732	2162.7	16.194	1280.6
1510	1.1264	1.0648	1.1943	3077.7	NaN	NaN	22.746	2165.4	16.139	1281.3
1520	1.1250	1.0635	1.1921	3083.1	NaN	NaN	22.759	2168.1	16.086	1281.9
1530	1.1235	1.0621	1.1899	3088.5	NaN	NaN	22.772	2170.8	16.032	1282.6
1540	1.1221	1.0608	1.1878	3093.9	NaN	NaN	22.784	2173.5	15.979	1283.2
1550	1.1206	1.0595	1.1857	3099.3	NaN	NaN	22.797	2176.2	15.926	1283.9
1560	1.1192	1.0582	1.1836	3104.6	NaN	NaN	22.808	2178.9	15.874	1284.5
1570	1.1178	1.0569	1.1816	3110.0	NaN	NaN	22.820	2181.6	15.823	1285.1
1571	1.1177	1.0567	1.1814	3110.5	NaN	NaN	22.821	2181.8	15.818	1285.2
1580	1.1165	1.0556	1.1796	3115.3	NaN	NaN	22.831	2184.2	15.771	1285.7
1590	1.1151	1.0543	1.1777	3120.6	NaN	NaN	22.842	2186.9	15.721	1286.3
1600	1.1138	1.0531	1.1758	3125.9	NaN	NaN	22.853	2189.5	15.671	1286.9
1610	1.1125	1.0519	1.1740	3131.2	NaN	NaN	22.863	2192.2	15.621	1287.4
1620	1.1113	1.0507	1.1722	3136.5	NaN	NaN	22.873	2194.8	15.571	1288.0
1630	1.1100	1.0495	1.1704	3141.8	NaN	NaN	22.882	2197.4	15.523	1288.6
1640	1.1087	1.0484	1.1686	3147.0	NaN	NaN	22.892	2200.1	15.474	1289.1
1650	1.1075	1.0472	1.1669	3152.2	NaN	NaN	22.901	2202.7	15.426	1289.7
1660	1.1063	1.0461	1.1653	3157.5	NaN	NaN	22.909	2205.3	15.378	1290.2
1670	1.1051	1.0450	1.1636	3162.7	NaN	NaN	22.918	2207.9	15.331	1290.7
1671	1.1050	1.0449	1.1635	3163.2	NaN	NaN	22.919	2208.2	15.326	1290.7
1680	1.1039	1.0439	1.1621	3167.9	NaN	NaN	22.926	2210.5	15.284	1291.2
1690	1.1028	1.0428	1.1606	3173.1	NaN	NaN	22.934	2213.1	15.238	1291.6
1700	1.1017	1.0417	1.1591	3178.3	NaN	NaN	22.941	2215.7	15.192	1292.1
1710	1.1006	1.0407	1.1577	3183.5	NaN	NaN	22.949	2218.3	15.146	1292.5
1720	1.0995	1.0397	1.1563	3188.6	NaN	NaN	22.956	2220.9	15.101	1292.9

h(km)	γ_{ax}	γ_{D}	γ_{SD}	T_{m0}(K)	T_{m5}(K)	T_{m10}(K)	log(η_4) (Pa•s)	T_{ad}(K)	α ($10^{-6}K^{-1}$)	cp (J/(kg•K))
1730	1.0984	1.0387	1.1549	3193.8	NaN	NaN	22.962	2223.4	15.056	1293.4
1740	1.0974	1.0377	1.1536	3198.9	NaN	NaN	22.969	2226.0	15.012	1293.8
1750	1.0964	1.0367	1.1523	3204.1	NaN	NaN	22.975	2228.6	14.967	1294.2
1760	1.0954	1.0358	1.1511	3209.2	NaN	NaN	22.981	2231.1	14.924	1294.6
1770	1.0944	1.0349	1.1499	3214.3	NaN	NaN	22.986	2233.7	14.880	1294.9
1771	1.0943	1.0348	1.1498	3214.8	NaN	NaN	22.987	2233.9	14.876	1295.0
1780	1.0935	1.0340	1.1488	3219.4	NaN	NaN	22.992	2236.2	14.837	1295.3
1790	1.0926	1.0331	1.1478	3224.5	NaN	NaN	22.997	2238.8	14.795	1295.6
1800	1.0917	1.0322	1.1468	3229.6	NaN	NaN	23.002	2241.3	14.752	1295.9
1810	1.0908	1.0314	1.1458	3234.7	NaN	NaN	23.006	2243.9	14.711	1296.1
1820	1.0900	1.0305	1.1449	3239.7	NaN	NaN	23.010	2246.4	14.669	1296.3
1830	1.0892	1.0297	1.1440	3244.8	NaN	NaN	23.014	2248.9	14.628	1296.6
1840	1.0884	1.0290	1.1432	3249.8	NaN	NaN	23.018	2251.4	14.587	1296.9
1850	1.0876	1.0282	1.1424	3254.9	NaN	NaN	23.021	2254.0	14.546	1297.1
1860	1.0868	1.0274	1.1416	3259.9	NaN	NaN	23.024	2256.5	14.506	1297.3
1870	1.0861	1.0267	1.1409	3264.9	NaN	NaN	23.027	2259.0	14.466	1297.5
1871	1.0860	1.0266	1.1409	3265.5	NaN	NaN	23.027	2259.2	14.462	1297.5
1880	1.0854	1.0260	1.1403	3270.0	NaN	NaN	23.030	2261.5	14.427	1297.6
1890	1.0848	1.0253	1.1398	3275.0	NaN	NaN	23.032	2264.0	14.387	1297.7
1900	1.0841	1.0247	1.1393	3280.0	NaN	NaN	23.034	2266.5	14.348	1297.8
1910	1.0835	1.0240	1.1388	3285.0	NaN	NaN	23.035	2269.0	14.309	1297.8
1920	1.0830	1.0234	1.1385	3290.0	NaN	NaN	23.037	2271.5	14.271	1297.9
1930	1.0824	1.0228	1.1381	3295.0	NaN	NaN	23.037	2274.0	14.233	1297.9
1940	1.0818	1.0222	1.1377	3300.0	NaN	NaN	23.038	2276.5	14.195	1298.0
1950	1.0813	1.0216	1.1374	3305.0	NaN	NaN	23.039	2278.9	14.158	1298.0
1960	1.0808	1.0211	1.1372	3309.9	NaN	NaN	23.039	2281.4	14.120	1298.0
1970	1.0804	1.0206	1.1370	3314.9	NaN	NaN	23.038	2283.9	14.083	1297.9
1971	1.0803	1.0205	1.1370	3315.4	NaN	NaN	23.038	2284.1	14.080	1297.9
1980	1.0800	1.0201	1.1369	3319.9	NaN	NaN	23.038	2286.4	14.047	1297.8
1990	1.0796	1.0196	1.1369	3324.8	NaN	NaN	23.037	2288.9	14.010	1297.7
2000	1.0792	1.0192	1.1370	3329.8	NaN	NaN	23.035	2291.3	13.974	1297.5
2010	1.0789	1.0187	1.1371	3334.7	NaN	NaN	23.034	2293.8	13.938	1297.3
2020	1.0787	1.0183	1.1373	3339.7	NaN	NaN	23.032	2296.2	13.902	1297.1
2030	1.0784	1.0179	1.1374	3344.6	NaN	NaN	23.030	2298.7	13.867	1296.9
2040	1.0781	1.0175	1.1376	3349.6	NaN	NaN	23.027	2301.2	13.832	1296.7
2050	1.0778	1.0172	1.1378	3354.5	NaN	NaN	23.024	2303.6	13.797	1296.5
2060	1.0776	1.0169	1.1381	3359.4	NaN	NaN	23.020	2306.1	13.762	1296.2
2070	1.0774	1.0166	1.1385	3364.4	NaN	NaN	23.017	2308.5	13.727	1295.9
2071	1.0774	1.0165	1.1386	3364.9	NaN	NaN	23.016	2308.8	13.724	1295.9
2080	1.0773	1.0163	1.1390	3369.3	NaN	NaN	23.012	2311.0	13.693	1295.5
2090	1.0772	1.0160	1.1395	3374.2	NaN	NaN	23.008	2313.4	13.659	1295.1
2100	1.0772	1.0158	1.1401	3379.1	NaN	NaN	23.003	2315.9	13.625	1294.7
2110	1.0772	1.0156	1.1408	3384.1	NaN	NaN	22.998	2318.3	13.591	1294.2
2120	1.0772	1.0154	1.1416	3389.0	NaN	NaN	22.992	2320.7	13.558	1293.7
2130	1.0772	1.0152	1.1422	3393.9	NaN	NaN	22.986	2323.2	13.524	1293.2
2140	1.0772	1.0151	1.1430	3398.8	NaN	NaN	22.979	2325.6	13.491	1292.8
2150	1.0772	1.0149	1.1438	3403.7	NaN	NaN	22.972	2328.1	13.458	1292.2
2160	1.0773	1.0148	1.1447	3408.6	NaN	NaN	22.964	2330.5	13.426	1291.7
2170	1.0774	1.0148	1.1457	3413.6	NaN	NaN	22.956	2332.9	13.393	1291.0
2171	1.0774	1.0148	1.1458	3414.1	NaN	NaN	22.955	2333.2	13.390	1291.0
2180	1.0776	1.0147	1.1467	3418.5	NaN	NaN	22.948	2335.4	13.361	1290.4
2190	1.0778	1.0147	1.1478	3423.4	NaN	NaN	22.939	2337.8	13.328	1289.7
2200	1.0781	1.0147	1.1490	3428.3	NaN	NaN	22.929	2340.2	13.296	1288.9
2210	1.0784	1.0147	1.1503	3433.2	NaN	NaN	22.919	2342.6	13.264	1288.1
2220	1.0787	1.0147	1.1516	3438.2	NaN	NaN	22.909	2345.1	13.233	1287.3
2230	1.0790	1.0148	1.1529	3443.1	NaN	NaN	22.898	2347.5	13.201	1286.5
2240	1.0793	1.0148	1.1542	3448.0	NaN	NaN	22.887	2349.9	13.170	1285.7
2250	1.0797	1.0150	1.1556	3452.9	NaN	NaN	22.875	2352.4	13.138	1284.9
2260	1.0801	1.0151	1.1571	3457.9	NaN	NaN	22.862	2354.8	13.107	1284.0
2270	1.0805	1.0152	1.1587	3462.8	NaN	NaN	22.849	2357.2	13.076	1283.1
2271	1.0805	1.0152	1.1588	3463.3	NaN	NaN	22.847	2357.4	13.073	1283.0
2280	1.0810	1.0154	1.1603	3467.7	NaN	NaN	22.835	2359.6	13.045	1282.1
2290	1.0815	1.0156	1.1620	3472.6	NaN	NaN	22.821	2362.1	13.014	1281.0
2300	1.0821	1.0158	1.1638	3477.6	NaN	NaN	22.806	2364.5	12.983	1279.9

h(km)	γ_{ax}	γ_{D}	γ_{SD}	T_{m0}(K)	T_{mS}(K)	T_{m10}(K)	log(η_4) (Pa•s)	T_{ad}(K)	α ($10^{-6}K^{-1}$)	cp (J/(kg•K))
2310	1.0827	1.0161	1.1657	3482.5	NaN	NaN	22.790	2366.9	12.953	1278.8
2320	1.0834	1.0163	1.1677	3487.5	NaN	NaN	22.774	2369.3	12.922	1277.6
2330	1.0840	1.0166	1.1695	3492.4	NaN	NaN	22.758	2371.8	12.892	1276.5
2340	1.0846	1.0169	1.1714	3497.4	NaN	NaN	22.740	2374.2	12.861	1275.4
2350	1.0853	1.0173	1.1734	3502.3	NaN	NaN	22.722	2376.6	12.831	1274.2
2360	1.0860	1.0176	1.1755	3507.3	NaN	NaN	22.703	2379.0	12.801	1273.0
2370	1.0867	1.0180	1.1777	3512.2	NaN	NaN	22.684	2381.5	12.771	1271.7
2371	1.0868	1.0180	1.1779	3512.7	NaN	NaN	22.682	2381.7	12.768	1271.5
2380	1.0875	1.0184	1.1799	3517.2	NaN	NaN	22.664	2383.9	12.741	1270.3
2390	1.0884	1.0188	1.1822	3522.2	NaN	NaN	22.643	2386.3	12.711	1268.9
2400	1.0893	1.0193	1.1846	3527.2	NaN	NaN	22.621	2388.8	12.681	1267.5
2410	1.0902	1.0198	1.1871	3532.2	NaN	NaN	22.599	2391.2	12.651	1266.0
2420	1.0912	1.0203	1.1897	3537.1	NaN	NaN	22.576	2393.6	12.622	1264.4
2430	1.0921	1.0208	1.1921	3542.1	NaN	NaN	22.552	2396.1	12.592	1263.0
2440	1.0930	1.0213	1.1946	3547.1	NaN	NaN	22.527	2398.5	12.562	1261.5
2450	1.0940	1.0219	1.1972	3552.2	NaN	NaN	22.502	2400.9	12.533	1260.0
2460	1.0950	1.0225	1.1999	3557.2	NaN	NaN	22.476	2403.4	12.503	1258.4
2470	1.0961	1.0231	1.2026	3562.2	NaN	NaN	22.449	2405.8	12.474	1256.7
2471	1.0962	1.0232	1.2029	3562.7	NaN	NaN	22.446	2406.1	12.471	1256.6
2480	1.0972	1.0238	1.2055	3567.3	NaN	NaN	22.421	2408.3	12.444	1255.0
2490	1.0984	1.0244	1.2084	3572.3	NaN	NaN	22.392	2410.7	12.415	1253.3
2500	1.0996	1.0251	1.2114	3577.4	NaN	NaN	22.362	2413.1	12.385	1251.5
2510	1.1009	1.0258	1.2145	3582.4	NaN	NaN	22.331	2415.6	12.356	1249.6
2520	1.1022	1.0266	1.2177	3587.5	NaN	NaN	22.300	2418.1	12.326	1247.6
2530	1.1034	1.0273	1.2207	3592.6	NaN	NaN	22.267	2420.5	12.297	1245.8
2540	1.1047	1.0281	1.2238	3597.6	NaN	NaN	22.234	2423.0	12.267	1244.0
2550	1.1060	1.0289	1.2269	3602.8	NaN	NaN	22.200	2425.4	12.238	1242.1
2560	1.1073	1.0297	1.2302	3607.9	NaN	NaN	22.164	2427.9	12.208	1240.1
2570	1.1087	1.0306	1.2335	3613.0	NaN	NaN	22.128	2430.3	12.179	1238.1
2571	1.1088	1.0307	1.2339	3613.5	NaN	NaN	22.124	2430.6	12.176	1237.9
2580	1.1101	1.0315	1.2370	3618.1	NaN	NaN	22.090	2432.8	12.149	1236.0
2590	1.1116	1.0324	1.2405	3623.2	NaN	NaN	22.052	2435.3	12.120	1233.9
2600	1.1132	1.0333	1.2441	3628.4	NaN	NaN	22.012	2437.8	12.090	1231.7
2610	1.1148	1.0342	1.2478	3633.6	NaN	NaN	21.972	2440.2	12.061	1229.4
2620	1.1165	1.0352	1.2516	3638.8	NaN	NaN	21.930	2442.7	12.031	1227.1
2630	1.1180	1.0362	1.2553	3643.9	NaN	NaN	21.887	2445.2	12.001	1224.9
2640	1.1195	1.0372	1.2589	3649.1	NaN	NaN	21.843	2447.7	11.972	1222.7
2650	1.1212	1.0382	1.2627	3654.3	NaN	NaN	21.798	2450.2	11.942	1220.4
2660	1.1228	1.0393	1.2665	3659.6	NaN	NaN	21.752	2452.6	11.912	1218.0
2670	1.1246	1.0404	1.2705	3664.8	NaN	NaN	21.704	2455.1	11.882	1215.6
2671	1.1247	1.0405	1.2709	3665.3	NaN	NaN	21.699	2455.4	11.879	1215.4
2680	1.1263	1.0415	1.2745	3670.1	NaN	NaN	21.655	2457.6	11.852	1213.1
2690	1.1282	1.0426	1.2787	3675.3	NaN	NaN	21.605	2460.1	11.822	1210.6
2700	1.1301	1.0438	1.2829	3680.6	NaN	NaN	21.554	2462.6	11.792	1208.0
2710	1.1320	1.0449	1.2872	3685.9	NaN	NaN	21.501	2465.2	11.761	1205.3
2720	1.1340	1.0461	1.2916	3691.2	NaN	NaN	21.447	2467.7	11.731	1202.6
2730	1.1360	1.0474	1.2961	3696.5	NaN	NaN	21.392	2470.2	11.701	1199.8
2740	1.1381	1.0486	1.3007	3701.9	NaN	NaN	21.336	2472.7	11.670	1197.0
2741	1.1384	1.0487	1.3012	3702.4	NaN	NaN	21.330	2473.0	11.667	1196.7
2741	1.1384	0.3365	0.2547	3702.4	NaN	NaN	21.330	2473.0	11.667	1196.7
2750	1.1406	0.3362	0.2549	3707.2	NaN	NaN	21.278	2475.2	11.644	1192.6
2760	1.1427	0.3360	0.2551	3712.6	NaN	NaN	21.218	2477.8	11.618	1188.4
2770	1.1445	0.3357	0.2554	3718.1	NaN	NaN	21.157	2480.3	11.593	1184.6
2771	1.1447	0.3357	0.2554	3718.6	NaN	NaN	21.151	2480.6	11.590	1184.2
2780	1.1460	0.3354	0.2557	3723.5	NaN	NaN	21.095	2482.9	11.567	1181.1
2790	1.1472	0.3351	0.2560	3728.9	NaN	NaN	21.031	2485.5	11.542	1178.0
2800	1.1481	0.3349	0.2564	3734.4	NaN	NaN	20.966	2488.0	11.516	1175.2
2810	1.1486	0.3346	0.2568	3739.9	NaN	NaN	20.900	2490.6	11.491	1172.7
2820	1.1488	0.3343	0.2572	3745.4	NaN	NaN	20.831	2493.2	11.466	1170.6
2830	1.1488	0.3340	0.2572	3750.9	NaN	NaN	20.761	2495.8	11.441	1168.8
2840	1.1483	0.3337	0.2572	3756.4	NaN	NaN	20.690	2498.4	11.416	1167.4
2850	1.1476	0.3334	0.2572	3762.0	NaN	NaN	20.617	2501.0	11.391	1166.3
2860	1.1465	0.3331	0.2573	3767.5	NaN	NaN	20.542	2503.6	11.366	1165.5
2870	1.1451	0.3328	0.2574	3773.1	NaN	NaN	20.466	2506.2	11.342	1165.0

h(km)	γ_{ax}	γ_D	γ_{SD}	T_{m0}(K)	T_{m5}(K)	T_{m10}(K)	log(η_4) (Pa•s)	T_{ad}(K)	α ($10^{-6}K^{-1}$)	cp (J/(kg•K))
2871	1.1450	0.3328	0.2574	3773.6	NaN	NaN	20.458	2506.4	11.339	1165.0
2880	1.1434	0.3325	0.2575	3778.6	NaN	NaN	20.388	2508.8	11.317	1164.9
2885	1.1425	0.3324	0.2575	3781.4	NaN	NaN	20.348	2510.1	11.305	1165.0
2890	1.1414	0.3322	0.2576	3784.2	NaN	NaN	20.308	2511.4	11.292	1165.2
2891	1.1412	0.3322	0.2576	3784.8	NaN	NaN	20.300	2511.6	11.290	1165.2

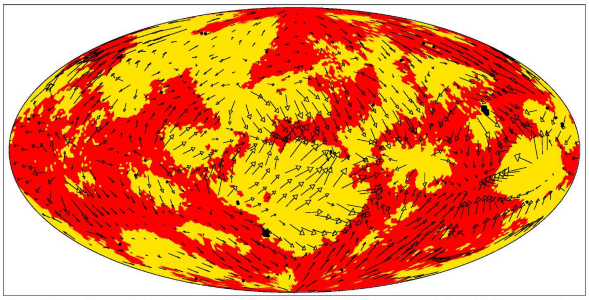

Run 591 f3 = 0.991 σ_y = 120 MPa r_n = 0.50 meridian 180° midmost
Age = 0.0000 Ma Max vel = 1.388 cm/a Av hor vel = 0.459 cm/a

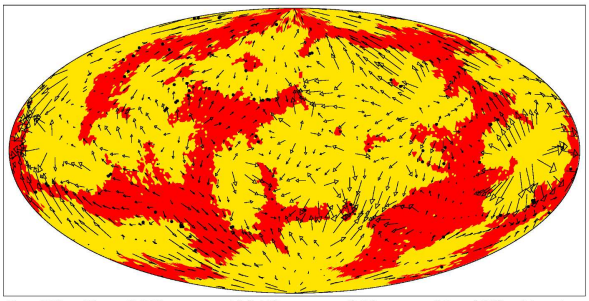

Run 580 f3 = 0.989 σ_y = 120 MPa r_n = 0.50 meridian 180° midmost
Age = 0.0000 Ma Max vel = 1.725 cm/a Av hor vel = 0.536 cm/a

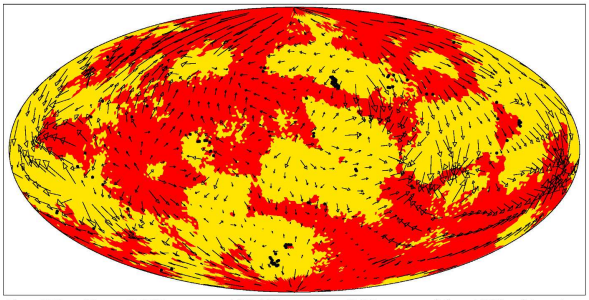

Run 581 f3 = 0.987 σ_y = 120 MPa r_n = 0.50 meridian 180° midmost
Age = 0.0000 Ma Max vel = 1.481 cm/a Av hor vel = 0.486 cm/a

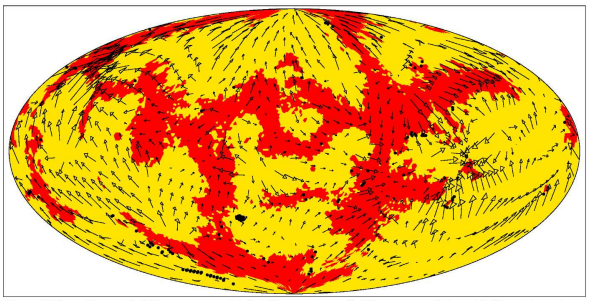

Run 592 f3 = 0.985 σ_y = 120 MPa r_n = 0.50 meridian 180° midmost
Age = 0.0000 Ma Max vel = 1.712 cm/a Av hor vel = 0.663 cm/a

Fig. B3. Present-day distribution of continents (red), oceanic lithosphere (yellow), and oceanic plateaus (black dots). These diagrams are based on, from top to bottom, f_3 values of 0.991, 0.989, 0.987, and 0.985, respectively. All four diagrams have constant r_n (0.5), σ_y (120 MPa), and k (5.0 W/(m·K)) values. Arrows signify present-day surface creep velocities.

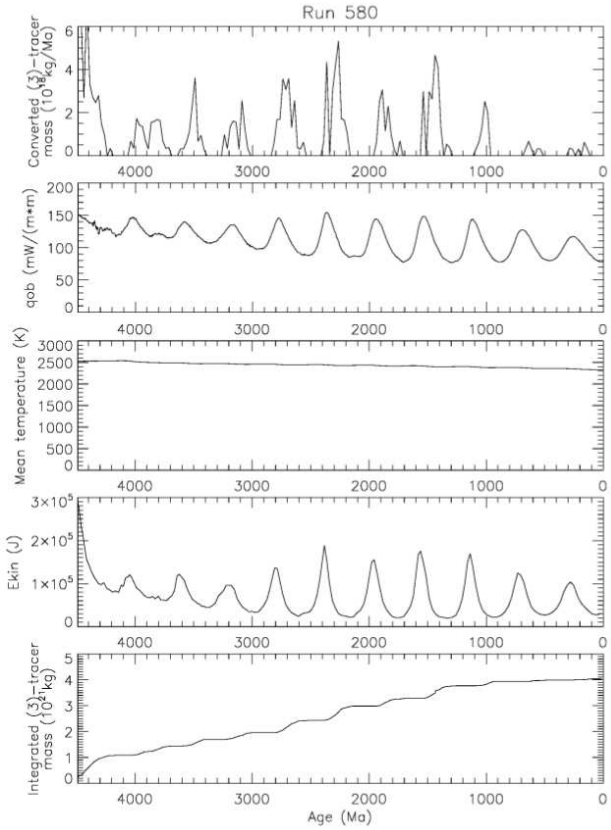

Fig. B4. *Typical* run (Run 580) of the model discussed in this study. The first panel represents episodes of juvenile magmatic activity, whereas the second panel displays the laterally averaged heat flow (*qob*) at the Earth's surface. The third panel shows volumetrically averaged temperatures (T_{mean}) as a function of age, and the fourth shows the kinetic energy of solid-state creep convection in the mantle (E_{kin}). Finally, the growth of the integrated mass of all of the continents is represented by the fifth graph. It should be noted that this run is shown as an example and that the run with the best agreement with the observed parameters (case 498) is not shown in this paper.

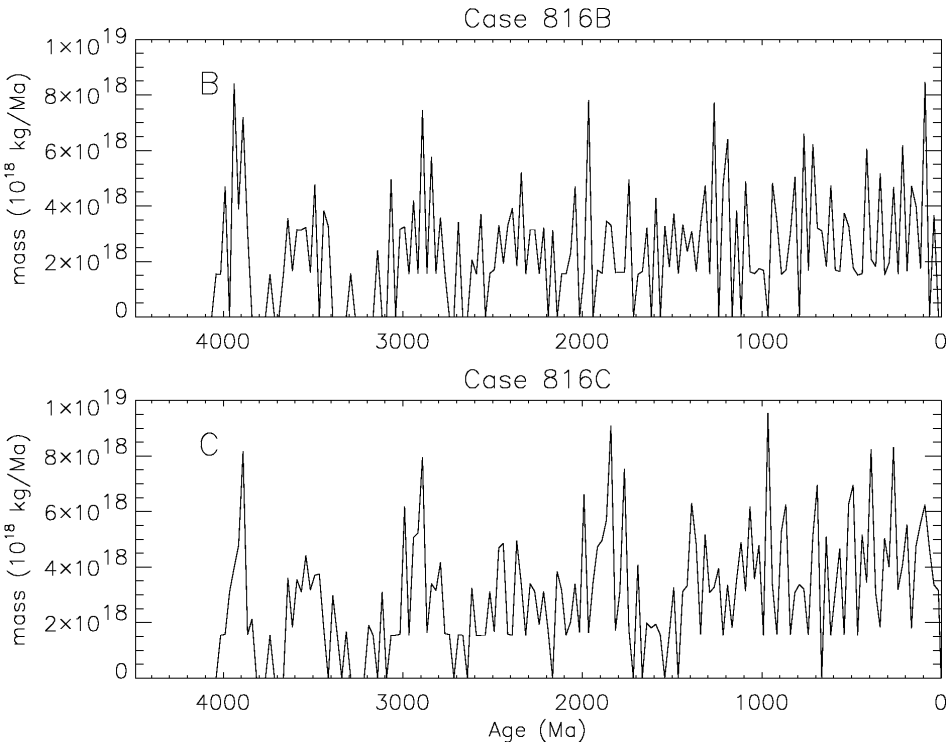

Fig. B5. Temporal distribution of juvenile contributions to the total mass of the continents for two cases (a B-run in the upper panel and a C-run in the lower panel) run without a water-dependent solidus. The rate of the converted continental-tracer mass was averaged over 25 Ma and is plotted in a discretised form after converting into units of 10^{18} kg/Ma.

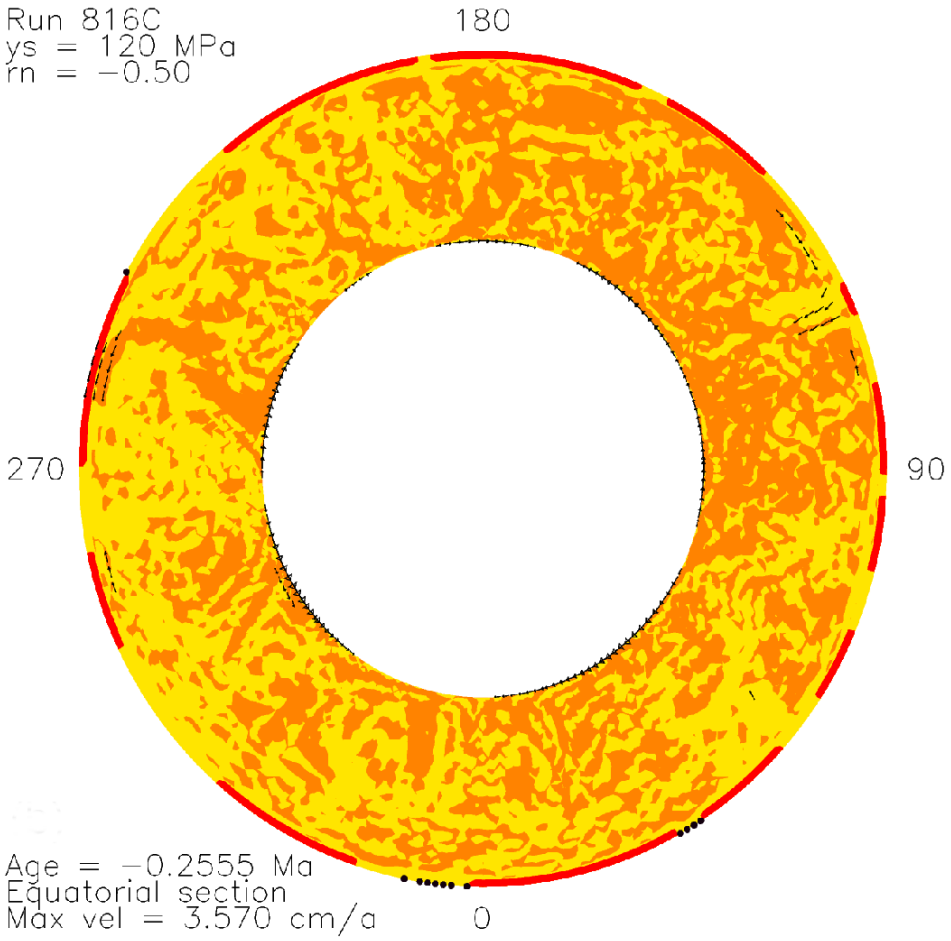

Fig. B6. Equatorial section through the mantle showing the present-day state of the chemical evolution of incompatible elements of the Earth's mantle for a case without a water-dependent solidus. Depleted mantle (DM) and mantle sections that are enriched in incompatible elements are strongly intermixed, with mantle volumes with more than 50% DM coloured yellow and relatively enriched sections with less than 50% DM coloured orange. In general, the yellow–orange boundary does not correspond to any discontinuity in U, Th, or K abundances. This model has a yield stress of 120 Pa and a viscosity level parameter value of –0.50. Very high creep rates are denoted by arrows.

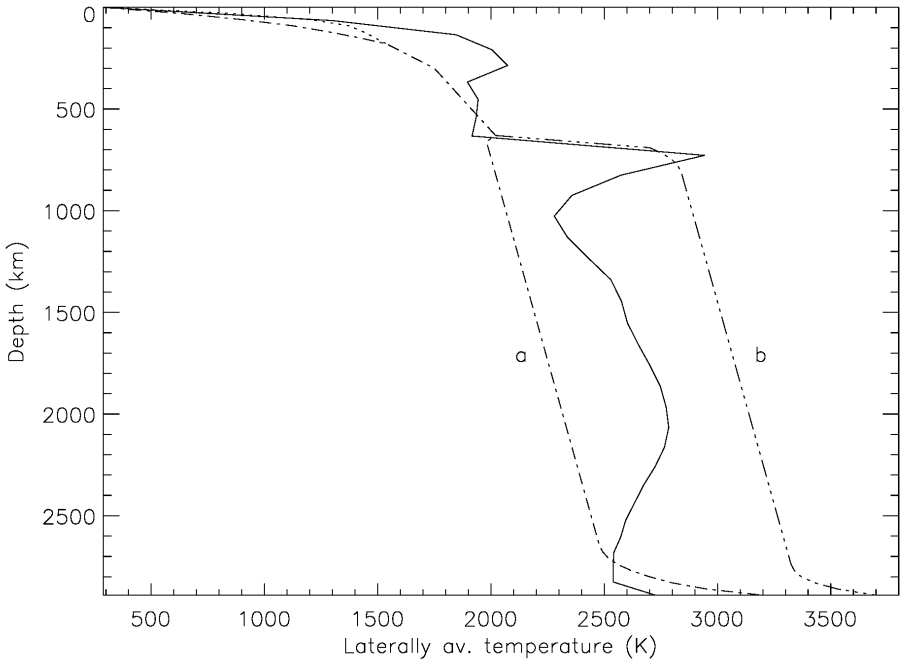

Fig. B7. Laterally averaged mantle temperature profile (solid line) during the final period of nearly separate bulk convection circulation in case 498. A range of mantle geotherms from parameterised evolution models (Schubert et al., 2001) is shown as dashed lines for comparison, where a and b denote geotherms relating to whole-mantle and layered convection, respectively. av. stands for averaged.

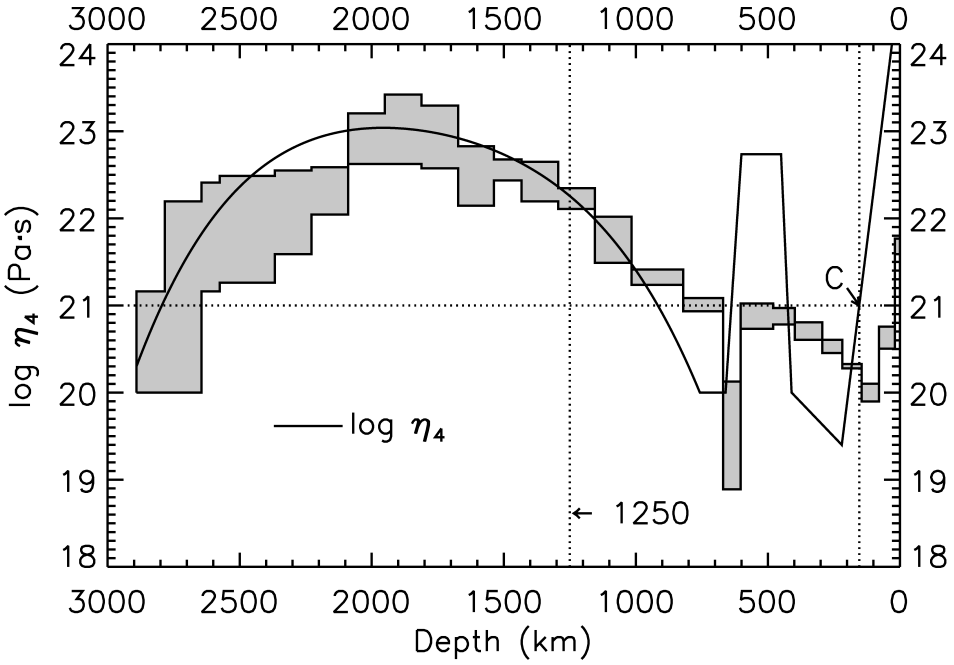

Fig. B8. Comparison of the viscosity function (η_4) derived in this study (solid line) with the mantle viscosity profile of Mitrovica and Forte (2004). The shading denotes the error bars of the model of Mitrovica and Forte (2004). The depth C is defined by the first coincidence of our viscosity function with 10^{21} Pa·s. Averaging of our viscosity function between the depth values C and 1250 km yields 10^{21} Pa·s.

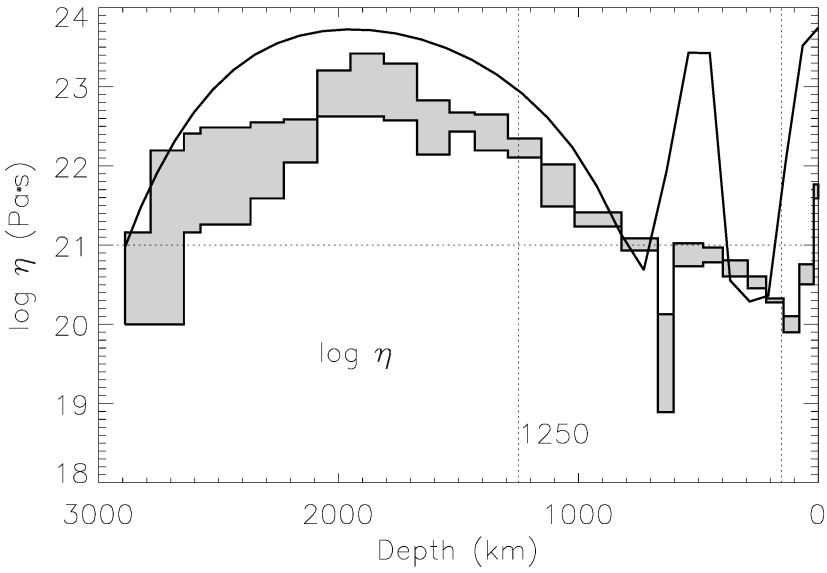

Fig. B9. Comparison of the present-day viscosity obtained from case 498 (solid line) with the viscosity derived by Mitrovica and Forte (2004).

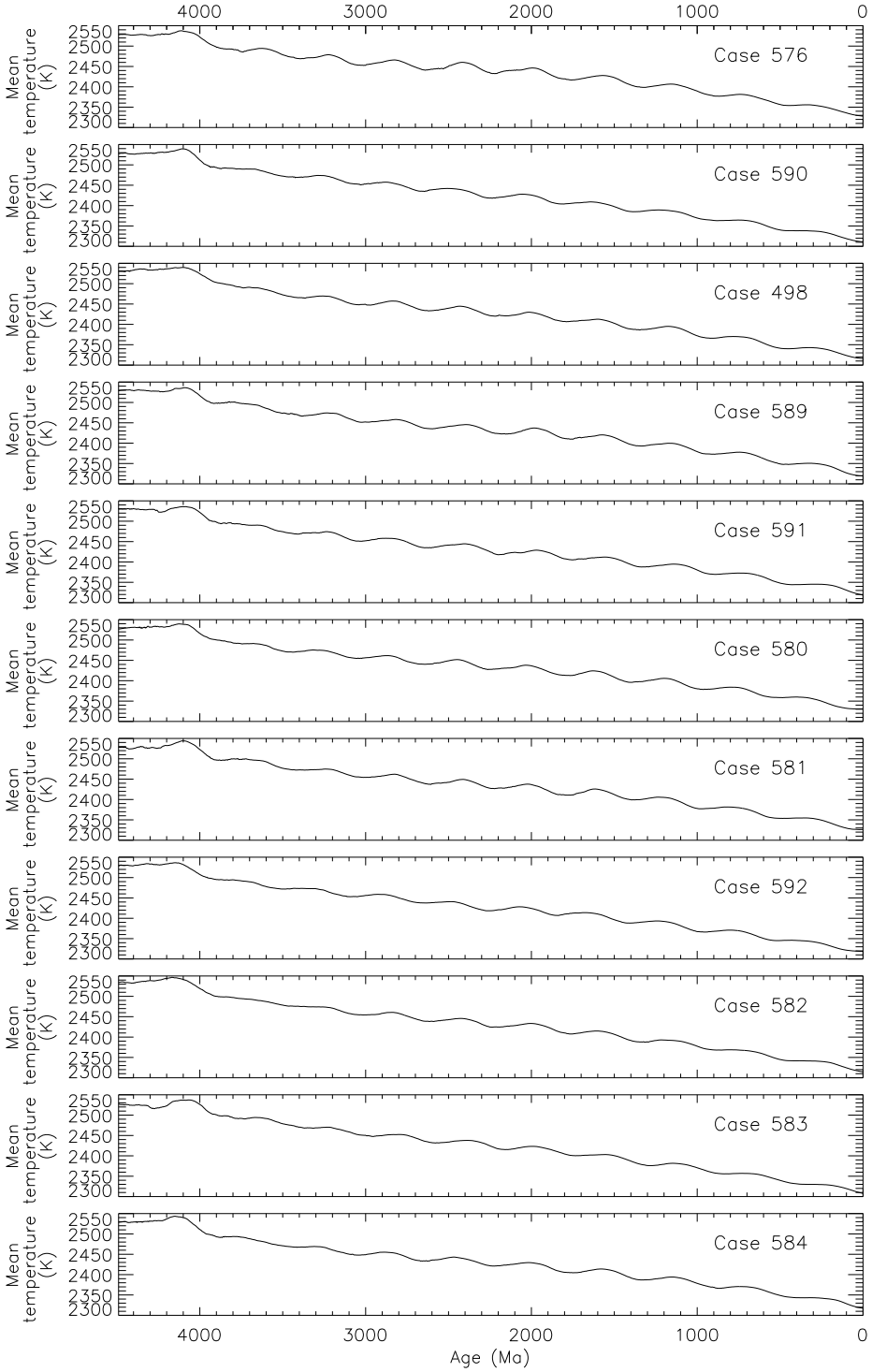

Fig. B10. Evolution of volumetrically averaged temperature values between $\tau = 4490$ Ma and the present day. This modelling employed variations in the melting-criterion parameter (f_3) between 0.999 (top panel) and 0.979 (bottom panel) in steps of 0.002, with σ_y (120 MPa),r_n (0.5), and k (5.0 W/(m·K)) values kept constant.

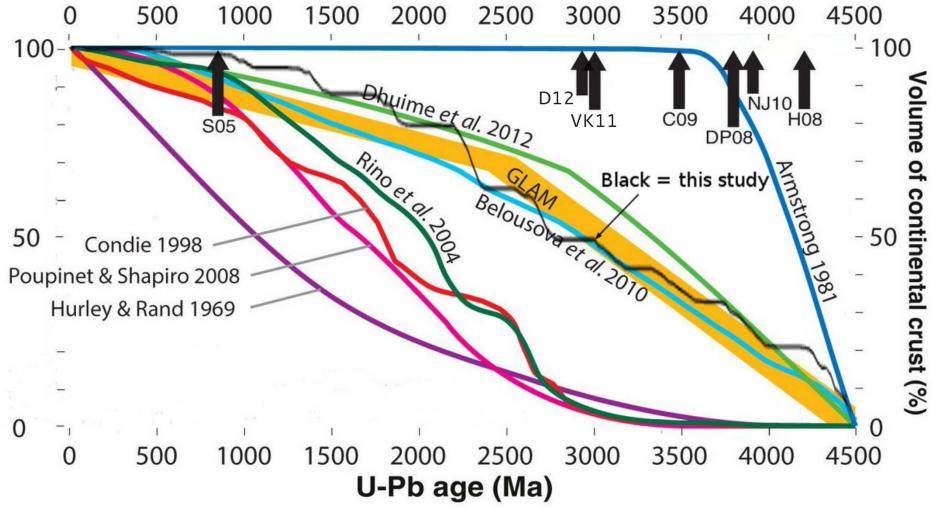

Fig. B11. Models of continental growth over time, extended from fig. 2(a) in Roberts and Spencer (2015). This diagram shows the integrated volume of the continental crust as a function of age. The black curve is our purely computational result (run 498) based on a solution of the physical balance equations plus a simplified model of crust–mantle differentiation that is dependent on generally accepted geochemical observations. Comparisons with other observational findings indicates that the run shown in this diagram produces the optimal results. Our black curve resembles other modern crustal growth curves (GLAM, Global Lithospheric Mapping, Begg et al. (2009), Belousova et al. (2010), Dhuime et al. (2012)), with our modelling yielding a pronounced *episodicity*. Estimates of the timing of the onset of modern-style subduction are indicated by black arrows (H08, Hopkins et al. (2008); NJ10, Nebel-Jacobsen et al. (2010); DP08, Dilek and Polat (2008); C09, Chen et al. (2009); VK11, van Kranendonk (2011); D12, Dhuime et al. (2012); S05, Stern (2005). The vertical axis denotes the percentage of present-day continental crust volume.

Table B2. Columns 2–8 show our computational results, where the presence of a subscript 9 indicates that the six values are averaged over the past 900 Ma. For example, qob_9 is based on qob, the laterally averaged surface heat flow, q_{c9} on q_c, the laterally averaged CMB heat flow, E_{kin9} on E_{kin}, the kinetic energy of the convective flow, T_{mean9} on T_{mean}, the volumetrically averaged mantle temperature, $q_{ob,t9}$ on $q_{ob,t}$, the total surface heat flow, and $q_{c,t9}$ on $q_{c,t}$, the total CMB heat flow. The quantity p_{t25} is the percentage of the present-day continental area that existed at $\tau = 2500$ Ma.

Case	qob_9 (mW/m^2)	q_{c9} (mW/m^2)	E_{kin9} (10^5 J)	T_{mean9} (K)	$q_{ob,t9}$	$q_{c,t9}$ (TW)	p_{t25} (%)
576	96.69	23.77	0.5518	2359	49.32	3.617	63.51
590	94.50	17.42	0.5356	2343	48.20	2.651	70.21
498	95.42	19.09	0.5677	2346	48.67	2.905	70.99
589	96.34	20.07	0.5697	2353	49.14	3.055	63.35
591	95.51	19.25	0.5656	2351	48.71	2.930	70.02
580	97.29	23.60	0.5745	2359	49.62	3.592	60.39
581	96.64	19.93	0.5705	2356	49.29	3.033	69.30
592	94.77	19.69	0.5531	2346	48.34	2.996	64.20
582	95.16	17.50	0.5460	2347	48.54	2.663	65.23
583	93.45	17.76	0.5399	2338	47.67	2.703	75.68
584	95.39	22.02	0.5734	2350	48.66	3.351	61.62
Av. of the 11 values	95.56	20.01	0.5589	2350	48.74	3.045	66.77

Table B3. Columns 2–4 present volumetrically averaged mantle temperatures at the beginning of the evolution of the *crystalline* Earth's mantle ($T_{mean,beg}$), the present-day volumetrically averaged mantle ($T_{mean,end}$), and the difference between the two ($\Delta T_{mean} = T_{mean,beg} - T_{mean,end}$) for the same sequence of runs as listed in Table B2.

Case	Tmean,beg	Tmean,end	ΔTmean
576	2528	2328	199.8
590	2527	2311	216.4
498	2531	2316	214.8
589	2529	2320	208.9
591	2530	2319	211.3
580	2527	2331	196.0
581	2528	2327	201.5
592	2529	2319	210.0
582	2534	2315	219.2
583	2527	2308	219.2
584	2528	2317	211.0

Table B4. Model parameters

Parameter	Description	Value	
r_{min}	Inner radius of spherical shell	3.480×10^6	m
r_{max}	Outer radius of spherical shell	6.371×10^6	m
	Temperature at the shell boundary	288	K
h_1	Depth of the exothermic phase boundary	4.10×10^5	m
h_2	Depth of the endothermic phase boundary	6.60×10^5	m
γ_1	Clausius–Clapeyron slope for the olivine–wadsleyite transition	$+1.6 \times 10^6$	$Pa \cdot K^{-1}$
γ_2	Clausius–Clapeyron slope for the ringwoodite–perovskite transition	-2.5×10^6	$Pa \cdot K^{-1}$
f_{a1}	Non-dimensional density jump for the olivine–wadsleyite transition	0.0547	
f_{a2}	Non-dimensional density jump for the ringwoodite–perovskite transition	0.0848	
	Begin of the thermal evolution of the *solid* Earth's silicate mantle	4.490×10^9	a
d_1	Non-dimensional transition width for the olivine–wadsleyite transition	0.05	
d_2	Non-dimensional transition width for the ringwoodite–perovskite transition	0.05	
	Begin of the radioactive decay	4.565×10^9	a
c_t	Factor of the lateral viscosity variation	1	
k	Thermal conductivity	5	$W \cdot m^{-1} \cdot K^{-1}$
$nr + 1$	Number of radial levels	33	
	Number of gridpoints	1.351746×10^6	

References

Begg, G., Griffin, W., Natapov, L., O'Reilly, S. Y., Grand, S., O'Neill, C., Hronsky, J., Djomani, Y. P., Swain, C., Deen, T., et al., 2009. The lithospheric architecture of Africa: seismic tomography, mantle petrology, and tectonic evolution. Geosphere 5 (1), 23–50.

Belousova, E., Reid, A., Griffin, W. L., O'Reilly, S. Y., 2009. Rejuvenation vs. recycling of Archean crust in the Gawler Craton, South Australia: Evidence from U–Pb and Hf isotopes in detrital zircon. Lithos 113 (3), 570–582.

Belousova, E. A., Kostitsyn, Y. A., Griffin, W. L., Begg, G. C., O'Reilly, S. Y., Pearson, N. J., 2010. The growth of the continental crust: Constraints from zircon Hf-isotope data. Lithos 119, 457–466.

Chen, B., Jahn, B., Tian, W., 2009. Evolution of the Solonker Suture Zone: constraints from zircon U–Pb ages, Hf isotopic ratios and whole-rock Nd–Sr isotope compositions of subduction- and collision-related magmas and forearc sediments. Journal of Asian Earth Sciences 34 (3), 245–257.

Christensen, U. R., Tilgner, A., 2004. Power requirement of the geodynamo from ohmic losses in numerical and laboratory dynamos. Nature 429 (6988), 169–171.

Davidson, J. P., Arculus, R. J., 2006. The significance of Phanerozoic arc magmatism in generating continental crust. In: Brown, M., Rushmer, T. (Eds.), Evolution and Differentiation of the Continental Crust. Cambridge University Press, Cambridge, UK, pp. 135–172.

Davies, G. F., 1988. Ocean bathymetry and mantle convection: 1. Large-scale flow and hotspots. Journal of Geophysical Research 93 (B9), 10467–10480.

Davies, G. F., 2006. Gravitational depletion of the early Earth's upper mantle and the viability of early plate tectonics. Earth and Planetary Science Letters 243, 376–382.

Davies, G. F., 2007. Controls on density stratification in the early mantle. Geochemistry, Geophysics, Geosystems 8, Q04006.

177 Dhuime, B., Hawkesworth, C. J., Cawood, P. A., Storey, C. D., 2012. A
178 change in the geodynamics of continental growth 3 billion years ago. Sci-
179 ence 335 (6074), 1334–1336.

180 Dilek, Y., Polat, A., 2008. Suprasubduction zone ophiolites and Archean
181 tectonics. Geology 36 (5), 431–432.

182 Dziewonski, A. M., Anderson, D. L., 1981. Preliminary reference Earth
183 model. Physics of the Earth and Planetary Interiors 25, 297–356.

184 Griffin, W., OReilly, S., Afonso, J., Begg, G., 2010. The evolution and ex-
185 tent of Archean continental lithosphere: Implications for tectonic models.
186 In: Planet Formation, Crustal Growth and the Evolving Lithosphere: 5th
187 International Archean Symposium. pp. 21–24.

188 Hopkins, M., Harrison, T. M., Manning, C. E., 2008. Low heat flow inferred
189 from $>$ 4 Gyr zircons suggests Hadean plate boundary interactions. Nature
190 456 (7221), 493–496.

191 Labrosse, S., Jaupart, C., 2007. Thermal evolution of the Earth: Secular
192 changes and fluctuations of plate characteristics. Earth and Planetary Sci-
193 ence Letters 260 (3), 465–481.

194 Litasov, K. D., 2011. Physicochemical conditions for melting in the Earth's
195 mantle containing a C-O-H fluid (from experimental data). Russian Geol-
196 ogy and Geophysics 52, 475–492.

197 Martin, H., Moyen, J.-F., Guitreau, M., Blichert-Toft, J., Le Pennec, J.-
198 L., 2014. Why Archaean TTG cannot be generated by MORB melting in
199 subduction zones. Lithos 198-199, 1–13.

200 Mitrovica, J. X., Forte, A. M., 2004. A new inference of mantle viscosity
201 based upon joint inversion of convection and glacial isostatic adjustment
202 data. Earth and Planetary Science Letters 225 (1), 177–189.

203 Monnereau, M., Yuen, D. A., 2010. Seismic imaging of the D" and constraints
204 on the core heat flux. Physics of the Earth and Planetary Interiors 180 (3),
205 258–270.

206 Nakagawa, T., Tackley, P. J., 2012. Influence of magmatism on mantle cool-
207 ing, surface heat flow and Urey ratio. Earth and Planetary Science Letters
208 329, 1–10.

209 Nakagawa, T., Tackley, P. J., 2015. Influence of plate tectonic mode on the
210 coupled thermochemical evolution of Earth's mantle and core. Geochem-
211 istry, Geophysics, Geosystems 16 (10), 3400–3413.

212 Nebel-Jacobsen, Y., Münker, C., Nebel, O., Gerdes, A., Mezger, K., Nelson,
213 D. R., 2010. Reworking of Earth's first crust: constraints from Hf isotopes
214 in Archean zircons from Mt. Narryer, Australia. Precambrian Research
215 182 (3), 175–186.

216 Nimmo, F., 2007. Energetics of the core. Treatise on Geophysics 8, 31–65.

217 Roberts, N. M., Spencer, C. J., 2015. The zircon archive of continent for-
218 mation through time. Geological Society, London, Special Publications
219 389 (1), 197–225.

220 Schubert, G., Turcotte, D. L., Olson, T. R., 2001. Mantle Convection in the
221 Earth and Planets. Cambridge University Press, Cambridge, UK.

222 Sleep, N. H., 1990. Hotspots and mantle plumes: Some phenomenology. Jour-
223 nal of Geophysical Research 95 (B5), 6715–6736.

224 Stacey, F. D., Davis, P. M., 2009. Physics of the Earth, 4th Edition. Cam-
225 bridge University Press, Cambridge, UK.

226 Stern, R. J., 2005. Evidence from ophiolites, blueschists, and ultrahigh-
227 pressure metamorphic terranes that the modern episode of subduction
228 tectonics began in Neoproterozoic time. Geology 33 (7), 557–560.

229 Taylor, S. R., McLennan, S. M., 2009. Planetary Crusts: Their Composition,
230 Origin and Evolution. Cambridge University Press, Cambridge, UK.

231 van Hunen, J., van den Berg, A. P., 2008. Plate tectonics on the early Earth:
232 Limitations imposed by strength and buoyancy of subducted lithosphere.
233 Lithos 103 (1), 217–235.

234 van Hunen, J., van Keken, P. E., Hynes, A., Davies, G. F., 2008. Tectonics
235 of early Earth: Some geodynamic considerations. In: Condie, C., Pease,
236 V. (Eds.), When Did Plate Tectonics Begin on Planet Earth? Geological
237 Society of America, pp. 157–170.

van Kranendonk, M. J., 2011. Cool greenstone drips and the role of partial convective overturn in Barberton greenstone belt evolution. Journal of African Earth Sciences 60 (5), 346–352.

Walzer, U., Hendel, R., 2008. Mantle convection and evolution with growing continents. Journal of Geophysical Research 113, B09405.

Walzer, U., Hendel, R., Köstler, C., Kley, J., 2009. Andean Orogeny and Plate Generation. In: Nagel, W. E., Kröner, D. B., Resch, M. M. (Eds.), High Performance Computing in Science and Engineering '08. Springer, Berlin, pp. 559–583.